

Out-of-Distribution Detection with a Single Unconditional Diffusion Model

Alvin Heng¹, Alexandre H. Thiery², Harold Soh^{1,3}

¹Department of Computer Science, National University of Singapore

²Department of Statistics and Data Science, National University of Singapore

³Smart Systems Institute, National University of Singapore
{alvinh, harold}@comp.nus.edu.sg

Abstract

Out-of-distribution (OOD) detection is a critical task in machine learning that seeks to identify abnormal samples. Traditionally, unsupervised methods utilize a deep generative model for OOD detection. However, such approaches necessitate a different model when evaluating abnormality against a new distribution. With the emergence of foundational generative models, this paper explores whether a single generalist model can also perform OOD detection across diverse tasks. To that end, we introduce our method, Diffusion Paths, (DiffPath) in this work. DiffPath proposes to utilize a single diffusion model originally trained to perform unconditional generation for OOD detection. Specifically, we introduce a novel technique of measuring the rate-of-change and curvature of the diffusion paths connecting samples to the standard normal. Extensive experiments show that with a single model, DiffPath outperforms prior work on a variety of OOD tasks involving different distributions. Our code is publicly available at <https://github.com/clear-nus/diffpath>.

1 Introduction

Out-of-distribution (OOD) detection, or anomaly detection, seeks to detect abnormal samples that are drawn far from a given distribution. This is a vital problem as deep neural networks are known to be overconfident when making incorrect predictions on OOD samples [1, 2], leading to potential issues in safety-critical applications such as healthcare, finance and criminal justice [3]. Traditionally, OOD detection using only unlabeled data relies on training a generative model on in-distribution (ID) data. Thereafter, measures such as model likelihood or its variants are used as an OOD detection score [4–6]. An alternative approach is to utilize the excellent sampling capabilities of diffusion models (DMs) to reconstruct corrupted samples, and use the reconstruction loss as an OOD measure [7–9].

However, these conventional methods necessitate separate generative models tailored to specific ID datasets and require retraining if the ID data evolves, such as in continual learning setups. This prompts the question: can OOD detection be performed using a *single* generative model? We answer in the affirmative and present Diffusion Paths (DiffPath) in this paper. While the use of a single model for OOD detection has been proposed in the discriminative setting [10], to the best of our knowledge we are the first to explore this for generative models. We believe that the generative setting is particularly salient in light of recent trends where large foundational generative models achieve state-of-the-art (SOTA) results across various tasks [11, 12].

Our method utilizes a single DM trained on a diverse dataset (e.g., ImageNet). In a departure from prior works that utilize variants of likelihoods [6, 5, 4] or reconstruction losses [7–9], we propose to perform OOD detection by measuring characteristics of the forward diffusion trajectory, specifically its *rate-of-change* and *curvature*, which can be computed from the

score predicted by the diffusion model. We provide theoretical and empirical analyses that motivate these quantities as useful OOD detectors; their magnitudes are similar for samples from the same distribution and different otherwise. We summarize our contributions as follows:

1. We introduce a novel approach to OOD detection by examining the rate-of-change and curvature along the diffusion path connecting different distributions to standard normal.
2. Through comprehensive experiments with various OOD datasets, we show that a single generative model outperforms baselines that necessitates separate models for each distribution.
3. We offer a theoretical framework demonstrating that our method characterizes properties of the optimal transport (OT) path between the data distribution and the standard normal.

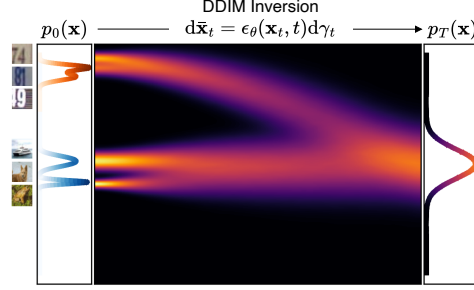


Figure 1: Illustration of the diffusion paths of two different datasets (CIFAR10 and SVHN) obtained via DDIM integration. The paths have different first and second derivatives (rate-of-change and curvature). We propose to measure these quantities for OOD detection.

2 Background

Score-based Diffusion Models. Let $p_0(\mathbf{x})$ denote the data distribution. We define a stochastic differential equation (SDE), also known as the forward process, to diffuse $p_0(\mathbf{x})$ to a noise distribution $p_T(\mathbf{x})$:

$$d\mathbf{x}_t = \mathbf{f}(\mathbf{x}_t, t)dt + g(t)d\mathbf{w}_t, \quad \mathbf{x}_0 \sim p_0(\mathbf{x}) \quad (1)$$

where $\mathbf{f}(\cdot, t) : \mathbb{R}^D \rightarrow \mathbb{R}^D$ is the drift coefficient, $g(t) \in \mathbb{R}$ is the diffusion coefficient and $\mathbf{w}_t \in \mathbb{R}^D$ is the standard Wiener process (Brownian motion). We denote p_t as the marginal distribution of Eq. 1 at time t . By starting from noise samples $\mathbf{x}_T \sim p_T$, new samples $\mathbf{x}_0 \sim p_0(\mathbf{x})$ can be sampled by simulating the reverse SDE

$$d\mathbf{x}_t = [\mathbf{f}(\mathbf{x}_t, t) - g(t)^2 \nabla_{\mathbf{x}} \log p_t(\mathbf{x}_t)]dt + g(t)d\bar{\mathbf{w}}_t, \quad \mathbf{x}_T \sim p_T(\mathbf{x}) \quad (2)$$

where $\bar{\mathbf{w}}_t$ is the standard Wiener process when time flows backwards from T to 0, and dt is an infinitesimal negative timestep. The diffusion process described by Eq. 1 also has an equivalent ODE formulation, termed the probability flow (PF) ODE [13], given by

$$d\mathbf{x}_t = \left[\mathbf{f}(\mathbf{x}_t, t) - \frac{1}{2}g(t)^2 \nabla_{\mathbf{x}} \log p_t(\mathbf{x}_t) \right] dt. \quad (3)$$

The ODE and SDE formulations are equivalent in the sense that trajectories under both processes share the same marginal distribution $p_t(\mathbf{x}_t)$. Hence, given an estimate of the score function $s_\theta(\mathbf{x}_t, t) \approx \nabla_{\mathbf{x}} \log p_t(\mathbf{x}_t)$, which can be obtained using score-matching approaches [14, 13], one can sample from the diffusion model by solving the reverse SDE or integrating the PF ODE backwards in time.

In this work, we focus on the variance-preserving formulation used in DDPM [15], which is given by an Ornstein-Uhlenbeck forward process

$$d\mathbf{x}_t = -\frac{1}{2}\beta_t \mathbf{x}_t dt + \sqrt{\beta_t} d\mathbf{w}_t, \quad \mathbf{x}_0 \sim p_0(\mathbf{x}) \quad (4)$$

where β_t are time-dependent constants. Under Eq. 4, diffused samples \mathbf{x}_t can be sampled analytically via $p_t(\mathbf{x}_t | \mathbf{x}_0) = \mathcal{N}(\mathbf{x}_t; \sqrt{\bar{\alpha}_t} \mathbf{x}_0, \sigma_t^2 \mathbf{I})$, where $\beta_t = -\frac{d}{dt} \log \bar{\alpha}_t$ and $\sigma_t^2 = 1 - \bar{\alpha}_t$. The score estimator, $\epsilon_\theta(\mathbf{x}_t, t) \approx -\sigma_t \nabla_{\mathbf{x}} \log p_t(\mathbf{x}_t)$, can be trained via the following objective

$$\min_{\theta} \mathbb{E}_{t \sim \mathcal{U}[0,1], \mathbf{x}_0 \sim p_0(\mathbf{x}_0), \mathbf{x}_t \sim p_t(\mathbf{x}_t | \mathbf{x}_0)} \left[\|\epsilon_\theta(\mathbf{x}_t, t) - \epsilon\|_2^2 \right], \quad (5)$$

where $\epsilon = -\sigma_t \nabla_{\mathbf{x}} \log p_t(\mathbf{x}_t | \mathbf{x}_0) = (\mathbf{x}_t - \sqrt{\bar{\alpha}_t} \mathbf{x}_0) / \sigma_t$.

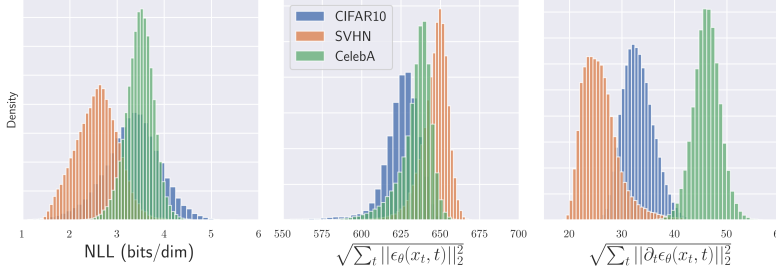


Figure 2: Histograms of various statistics of the respective training sets. The NLL is calculated using a diffusion model trained on CIFAR10, while the other two statistics are calculated with a model trained on ImageNet.

Table 1: AUROC of statistics shown in Fig. 2.

Method	C10 vs	
	SVHN	CelebA
NLL	0.091	0.573
$\sqrt{\sum_t \ \epsilon_\theta(\mathbf{x}_t, t)\ _2^2}$	0.856	0.638
$\sqrt{\sum_t \ \partial_t \epsilon_\theta(\mathbf{x}_t, t)\ _2^2}$	0.965	0.998

Unsupervised OOD Detection. We formalize the task of unsupervised OOD detection here. Given a distribution of interest $p(\mathbf{x})$, the goal of OOD detection is to construct a scoring function which outputs a quantity $S_\theta(\mathbf{x}) \in \mathbb{R}$ that identifies if a given test point \mathbf{x}_{test} is from $p(\mathbf{x})$. In this work, a higher value of $S_\theta(\mathbf{x}_{\text{test}})$ indicates that the sample is more likely to be drawn from $p(\mathbf{x})$. We will use the notation “A vs B” to denote the task of distinguishing samples between A and B, where A is the in-distribution (ID) and B is the out-of-distribution (OOD) dataset. In unsupervised OOD detection, one must construct the function S_θ using only knowledge of A.

3 Diffusion Models for OOD Detection

An overview of our method, DiffPath, is illustrated in Fig. 1. DiffPath is based on the insight that the *rate-of-change* and *curvature* of the diffusion path connecting samples to standard normal differ between distributions, making them effective indicators for OOD detection. This section outlines the methodology behind DiffPath. We begin in Sec. 3.1, where we provide evidence that likelihoods of a diffusion model are insufficient for OOD detection. Next, we show that the score function is a measure of the rate-of-change, as well as motivate the use of a single generative model in Sec. 3.2. Following which, we motivate the curvature as the derivative of the score in Sec. 3.3. We consider the curvature statistic as one variation of our method and abbreviate it as DiffPath-1D. In Sec. 3.4, we contextualize our method in terms of the optimal transport path between samples and standard normal, and finally propose a higher-order, hybrid variation called DiffPath-6D in Sec. 3.5, which incorporates both the rate-of-change and curvature quantities.

3.1 Likelihoods Do Not Work

When leveraging a likelihood-based generative model for OOD detection, the most natural statistic to consider is the likelihood itself. As DMs are trained to maximize the evidence lower bound (ELBO) of the data, one would expect that in-distribution samples have higher ELBO under the model compared to out-of-distribution samples. However, prior works [2, 16] have shown that the opposite behavior was observed in deep generative models, such as normalizing flows, where the model assigned higher likelihoods to OOD samples.

In Fig. 2, we plot the distributions of the negative ELBO (denoted NLL) of various training sets for a DM trained on CIFAR10. Our results corroborate earlier findings that likelihoods are not good OOD detectors; the NLL of CIFAR10 samples are higher than SVHN samples, meaning ID samples have lower likelihoods than OOD samples. Furthermore, the NLL of CIFAR10 overlaps significantly with that of CelebA samples. The poor AUROC score in Table 1 quantitatively demonstrates the inability of likelihoods to distinguish between ID and OOD samples. This motivates us to search for better statistics that we can extract from DMs for OOD detection.

3.2 Scores as OOD Statistic

Scores as KL Divergence Proxy. We start by rewriting the PF ODE, Eq. 3, in the following form:

$$\frac{d\mathbf{x}_t}{dt} = \mathbf{f}(\mathbf{x}_t, t) + \frac{g(t)^2}{2\sigma_t} \epsilon_p(\mathbf{x}_t, t) \quad (6)$$



Figure 3: Illustration of the forward integration of Eq. 7 on samples from CIFAR10, SVHN and CelebA. The ImageNet model is able bring the samples to approximately standard normal despite never being trained explicitly on them. The SVHN model is only able to bring the SVHN sample to standard normal. This highlights the necessity for the diffusion model to be trained on a large, diverse dataset so that it can estimate the scores for a variety of data accurately.

where we have parameterized the score as $\epsilon_p(\mathbf{x}_t, t) = -\sigma_t \nabla_{\mathbf{x}} \log p_t(\mathbf{x})$.

Theorem 1. Denote ϕ_t and ψ_t as the marginals from evolving two distinct distributions ϕ_0 and ψ_0 via their respective probability flow ODEs (Eq. 6) forward in time. We consider the case with the same forward process, i.e., the two PF ODEs have the same $\mathbf{f}(\mathbf{x}_t, t)$, $g(t)$ and σ_t . Under some regularity conditions stated in Appendix A.1,

$$D_{\text{KL}}(\phi_0 \parallel \psi_0) = \frac{1}{2} \int_0^T \mathbb{E}_{\mathbf{x} \sim \phi_t} \frac{g(t)^2}{\sigma_t} \|\epsilon_\phi(\mathbf{x}_t, t) - \epsilon_\psi(\mathbf{x}_t, t)\|_2^2 dt + D_{\text{KL}}(\phi_T \parallel \psi_T).$$

The term $D_{\text{KL}}(\phi_T \parallel \psi_T)$ vanishes as $\phi_T = \psi_T = \mathcal{N}(\mathbf{0}, \mathbf{I})$ by construction, assuming the true scores are available. In practice, one does not have access to the true score, and we rely on a score estimator ϵ_θ obtained via score matching approaches. Theorem 1 suggests that the scores of the marginal distributions along the ODE path serve as a proxy for the KL divergence: as $D_{\text{KL}}(\phi_0 \parallel \psi_0)$ increases, so should the difference in the norms of their scores. Another interpretation is that this difference, $\mathbb{E}[\|\epsilon_\phi(\mathbf{x}_t, t) - \epsilon_\psi(\mathbf{x}_t, t)\|_2^2]$, is a measure of the Fisher divergence between the two distributions, which forms the foundation for score matching [17]. Thus, this motivates the use of the norm of the scores as an OOD statistic in distinguishing two distributions apart.

However, Theorem 1 is not immediately useful as it requires a priori knowledge of both distributions, whereas in unsupervised OOD detection only knowledge of the in-distribution is available. Interestingly, we empirically observe that it is possible to approximate the forward probability flow ODE for different distributions using a *single* diffusion model when it is trained on a large, diverse dataset $p_0(\mathbf{x})$. Recall that as the PF ODE has the same marginal as the forward SDE, if the score estimate ϵ_θ has converged to the true score, then forward integration of a sample \mathbf{x}_0 using Eq. 6 should bring the sample to approximately standard normal, $\mathbf{x}_T \sim \mathcal{N}(\mathbf{0}, \mathbf{I})$.

Specifically, we consider the following parameterization [18] of the PF ODE

$$d\bar{\mathbf{x}}_t = \epsilon_\theta(\mathbf{x}_t, t) d\gamma_t \quad (7)$$

where $\gamma_t = \sqrt{\frac{1-\bar{\alpha}_t^2}{\bar{\alpha}_t}}$ and $\bar{\mathbf{x}}_t = \mathbf{x}_t \sqrt{1+\gamma_t^2}$. Let $\epsilon_\theta(\mathbf{x}_t, t) = -\sigma_t \nabla_{\mathbf{x}} \log p_t(\mathbf{x})$ be a score model trained on $p_0(\mathbf{x})$. It is known that the DDIM sampler [19] is Euler’s method applied to Eq. 7. In Fig. 3, we integrate Eq. 7 forward in time using DDIM for samples from distributions unseen by the model during training. We observe the surprising fact that when $p_0(\mathbf{x})$ is ImageNet, the model is able to bring the samples approximately to the standard normal. However, this is not true for the model trained on SVHN, suggesting that p_0 needs to be a large and diverse dataset. We ablate the choice of p_0 in Sec. 5.2.

This motivates ϵ_θ as a replacement for arbitrary ϵ_ϕ when integrating Eq. 7 forward with samples from ϕ_0 . In Fig. 2, we see that the distributions of $\sqrt{\sum_t \|\epsilon_\theta(\mathbf{x}_t, t)\|_2^2}$, the square root of the sum of L^2 norms of scores over time, applied to the three datasets using a single model trained on ImageNet are better separated than the likelihoods for CIFAR10 vs SVHN. We leverage this insight to design a simple scheme for OOD detection: fit a Kernel Density Estimator (KDE) to $\sqrt{\sum_t \|\epsilon_\theta(\mathbf{x}_t, t)\|_2^2}$ of the training set for a given distribution, then use the KDE likelihoods of a test sample as the OOD score S_θ . We provide pseudocode in Algorithm 1. The AUROC scores in Table 1 show a large improvement in CIFAR10 vs SVHN scores over likelihoods, although CIFAR10 vs CelebA is still lacking.

Algorithm 1 OOD detection with DiffPath

Input: Trained DM ϵ_θ , ID train set $\mathbf{X}_{\text{train}}$, test samples \mathbf{X}_{test} , empty lists L_{train} and L_{test}

Output: OOD scores of test samples $S_\theta(\mathbf{X}_{\text{test}})$

```
1: for  $\mathbf{x}_0$  in  $\mathbf{X}_{\text{train}}$  do
2:    $\{\epsilon_\theta(\mathbf{x}_t, t)\}_{t=0}^T \leftarrow \text{DDIMInversion}(\mathbf{x}_0, \epsilon_\theta)$   $\triangleright$  Integrate Eq. 7 from  $t = 0$  to  $T$ 
3:   Calculate OOD statistic using  $\{\epsilon_\theta(\mathbf{x}_t, t)\}_{t=0}^T$ 
4:   Append statistic to  $L_{\text{train}}$ 
5: end for
6:  $p_{\text{train}}(\cdot) \leftarrow$  fit density estimate to  $L_{\text{train}}$   $\triangleright$  e.g., KDE, GMM
7:  $L_{\text{test}} \leftarrow$  Repeat lines 1 – 5 with  $\mathbf{X}_{\text{test}}$ 
8: return  $p_{\text{train}}(l)$  for every  $l$  in  $L_{\text{test}}$ 
```

Score as First-Order Taylor Expansion. We provide a second interpretation of the score, and subsequently motivate a new statistic that can be used for OOD detection. Recall that the numerical DDIM solver is the first-order Euler’s method applied to Eq. 7. In general, we can expand the ODE to higher-order terms using the truncated Taylor method [20, 18]:

$$\begin{aligned}\bar{\mathbf{x}}_{t_{n+1}} &= \bar{\mathbf{x}}_{t_n} + h_n \frac{d\bar{\mathbf{x}}_{t_n}}{d\gamma_t} + \frac{1}{2} h_n^2 \frac{d^2 \bar{\mathbf{x}}_{t_n}}{d\gamma_t^2} \Big|_{(\bar{\mathbf{x}}_{t_n}, t_n)} + \dots \\ &= \bar{\mathbf{x}}_{t_n} + h_n \epsilon_\theta(\mathbf{x}_{t_n}, t_n) + \frac{1}{2} h_n^2 \frac{d\epsilon_\theta}{d\gamma_t} \Big|_{(\bar{\mathbf{x}}_{t_n}, t_n)} + \dots\end{aligned}\tag{8}$$

where $h_n = \gamma_{t_{n+1}} - \gamma_{t_n}$. The norm of the first-order score, $\|\epsilon_\theta\|_2$, therefore measures the *rate-of-change* of the ODE integration path. Intuitively, the ODE integration path necessary to bring different distributions to the standard normal in finite time differs (c.f. the PF ODE path is also the optimal transport path, see Sec. 3.4), hence the rate-of-change differs as well.

3.3 Second-Order Taylor Expansion (DiffPath-1D)

Based on the preceding discussion, it is natural to consider if higher-order terms in the ODE Taylor expansion can also serve as an effective OOD statistic. We answer in the affirmative by considering the second order term, $\frac{d\epsilon_\theta}{d\gamma_t}$. Intuitively, the second-order term measures the *curvature* of the ODE integration path. We expand the derivative as follows [18]:

$$\begin{aligned}\frac{d\epsilon_\theta}{d\gamma_t} &= \frac{\partial \epsilon_\theta(\mathbf{x}_t, t)}{\partial \mathbf{x}_t} \frac{d\mathbf{x}_t}{d\gamma_t} + \frac{\partial \epsilon_\theta(\mathbf{x}_t, t)}{\partial t} \frac{dt}{d\gamma_t} \\ &= \frac{1}{\sqrt{\gamma_t^2 + 1}} \underbrace{\frac{\partial \epsilon_\theta(\mathbf{x}_t, t)}{\partial \mathbf{x}_t} \epsilon_\theta(\mathbf{x}_t, t)}_{\text{JVP}} - \frac{\gamma_t}{1 + \gamma_t^2} \underbrace{\frac{\partial \epsilon_\theta(\mathbf{x}_t, t)}{\partial \mathbf{x}_t} \mathbf{x}_t}_{\text{JVP}} + \frac{\partial \epsilon_\theta(\mathbf{x}_t, t)}{\partial t} \frac{dt}{d\gamma_t}.\end{aligned}\tag{9}$$

We see that the derivative contains two Jacobian-Vector Products (JVP) and a simple time derivative term. In principle, all three terms can be computed using automatic differentiation. However, this makes inference twice as costly due to the need for an additional backward pass after every forward pass of the network, and significantly more memory-intensive due to storage of the full computation graph. Fortunately, the time derivative term can be computed using simple finite difference:

$$\frac{\partial \epsilon_\theta(\mathbf{x}_t, t)}{\partial t} \approx \frac{\epsilon_\theta(\mathbf{x}_{t+\Delta t}, t + \Delta t) - \epsilon_\theta(\mathbf{x}_t, t)}{\Delta t}\tag{10}$$

where the pairs $(\mathbf{x}_t, \mathbf{x}_{t+\Delta t})$ are obtained during standard DDIM integration. Thus, no additional costs associated with gradient computation are incurred.

Surprisingly, we observe that for high-dimensional distributions such as images that we consider in this work, the time derivative in Eq. 10 alone provides an accurate enough estimate for OOD detection. Using the same ImageNet model as in Sec. 3.2, we see from Fig. 2 that the distributions of $\sqrt{\sum_t \|\partial_t \epsilon_\theta(\mathbf{x}_t, t)\|_2^2}$ for different datasets are more spread out. This reflects quantitatively in the AUROC scores in Table 1, where the second-order statistic improves significantly upon the first-order scores, in particular for CIFAR10 vs CelebA with near perfect performance.

We thus consider the second-order statistic alone, $\sqrt{\sum_t \|\partial_t \epsilon_\theta(\mathbf{x}_t, t)\|_2^2}$, as one of our main statistic for OOD detection. As it is a one-dimensional quantity, we abbreviate it as DiffPath-1D.

3.4 Connections to Optimal Transport

Recent works have viewed DDIM integration as an encoder that maps the data distribution to standard normal [21, 22]. They prove that this map is the optimal transport (OT) path if the data distribution is Gaussian, while providing numerical results suggesting likewise for high-dimensional data like images. As a result, we can view the OOD statistics proposed in Sec. 3.2 and Sec. 3.3 as characterizing different derivatives of the OT path: the score $\|\epsilon_\theta\|_2$ represents the rate-of-change of the path, while the time derivative $\|\partial_t \epsilon_\theta\|_2$ represents its curvature.

To justify our proposition that derivatives of OT paths serve as meaningful OOD statistics, we consider the following toy example [21] of distinguishing two multivariate Gaussians (detailed derivation in Appendix A.2). Let the distributions be $p_0^i(\mathbf{x}) \sim \mathcal{N}(\mathbf{a}_i, \mathbf{I})$, $i \in \{0, 1\}$, where $\mathbf{a}_i \in \mathbb{R}^d$ and $\mathbf{I} \in \mathbb{R}^{d \times d}$. The marginal densities along the forward diffusion can be computed exactly using the transition formulas for SDEs [23] and is given by $p_t^i(\mathbf{x}) \sim \mathcal{N}(\mathbf{a}_i e^{-t}, \mathbf{I})$, with PF ODE $\frac{d\mathbf{x}_i}{dt} = -\mathbf{a}_i e^{-t}$. This path corresponds exactly to the OT map between p_0^i and $\mathcal{N}(\mathbf{0}, \mathbf{I})$. In this case, the corresponding first and second-order OOD statistics are equal and given by $\left\| \frac{d\mathbf{x}_i}{dt} \right\|_2 = \left\| \frac{d^2\mathbf{x}_i}{dt^2} \right\|_2 = \|\mathbf{a}_i e^{-t}\|_2$. Crucially, they are proportional to $\|\mathbf{a}_i\|_2$, meaning that as the two distributions move farther apart (i.e., as $\|\mathbf{a}_0 - \mathbf{a}_1\|_2$ increases), so should the L^2 norms of the OOD statistics, thereby increasing their ability to distinguish samples between the two.

3.5 Higher-dimensional Statistic (DiffPath-6D)

Owing to its simplicity, the one-dimensional statistic proposed in Sec. 3.3 may suffer from edge cases or perform suboptimally as information is condensed to a single scalar. For instance, given an image \mathbf{x}_0 with pixels normalized to the range $[-1, 1]$, one such edge case is distinguishing \mathbf{x}_0 from itself with the sign of the pixels flipped, $-\mathbf{x}_0$. The two samples will produce symmetric OT paths differing only by a negative sign, resulting in identical statistics after taking the L^2 norm. We can see this from Table 2 where DiffPath-1D fails to distinguish CIFAR10 samples from itself with signs flipped, which we call negative CIFAR10. As such, we are motivated to propose a higher-dimensional statistic that does not utilize the standard form of the L^p norm: $\|\mathbf{x}\|_p = \sum_i |\mathbf{x}_i|^p$. We define a new scalar quantity, $\langle \mathbf{x} \rangle_p = \sum_i (\mathbf{x}_i)^p$, which omits the absolute value so that sign information is retained, and propose a new six-dimensional statistic we dub DiffPath-6D:

Table 2: AUROC of DiffPath 1D vs 6D.

Method	C10 vs neg. C10
1D	0.500
6D	0.994

$$\left[\sum_t \langle \epsilon_\theta(\mathbf{x}_t, t) \rangle_1, \sum_t \langle \epsilon_\theta(\mathbf{x}_t, t) \rangle_2, \sum_t \langle \epsilon_\theta(\mathbf{x}_t, t) \rangle_3, \sum_t \langle \partial_t \epsilon_\theta(\mathbf{x}_t, t) \rangle_1, \sum_t \langle \partial_t \epsilon_\theta(\mathbf{x}_t, t) \rangle_2, \sum_t \langle \partial_t \epsilon_\theta(\mathbf{x}_t, t) \rangle_3 \right]^\top$$

which concatenates scalars based on the first, second and third powers of ϵ_θ and $\partial_t \epsilon_\theta$ into a vector. From Table 2, DiffPath-6D is able to distinguish CIFAR10 from neg. CIFAR10 near perfectly. We validate both DiffPath-1D and DiffPath-6D on a wider suite of experiments in Sec. 5.

4 Related Works

Modern OOD detection can be divided roughly into three categories: feature-based, likelihood-based, reconstruction-based. Feature-based methods extract features from ID samples and fit a likelihood or distance function as an OOD detector. For instance, one can obtain the latent representations of a test sample using an autoencoder and measure its Mahalanobis distance to the representations of ID samples [24]. Distances between features derived from self-supervised learning models are also utilized in similar contexts [25, 26]. Similar to our work, Xiao et al. [10] showed that one can perform OOD detection using features from a single discriminative model trained on ImageNet.

Likelihood-based approaches leverage a generative model trained on ID samples. These methods typically employ variants of the log-likelihood of a test sample under the model as the OOD detection score. Nalisnick et al. [2] first pointed out that deep generative models might erroneously assign higher likelihoods to OOD samples. Several explanations have been proposed, such as the input complexity [16] and typicality [27] of samples. As a result, just as we show in Sec. 3.1, vanilla likelihoods are rarely used. Instead, variants derived from the log-likelihood have been proposed, such as likelihood ratios [4], ensembles of the likelihood [5], density of states [6], energy-based models [28] and typicality tests [27]. A similar line of work to ours is MSMA [29], which uses the

Table 3: AUROC scores for various in-distribution vs out-of-distribution tasks. Higher is better. **Bold** and underline denotes the best and second best result respectively. We also show the number of function evaluations (NFE) for diffusion methods, where lower is better.

Method	C10 vs				SVHN vs				CelebA vs				Average	NFE
	SVHN	CelebA	C100	Textures	C10	CelebA	C100	Textures	C10	SVHN	C100	Textures		
IC	0.950	0.863	<u>0.736</u>	-	-	-	-	-	-	-	-	-	-	-
IGEBM	0.630	0.700	0.500	0.480	-	-	-	-	-	-	-	-	-	-
VAEBM	0.830	0.770	0.620	-	-	-	-	-	-	-	-	-	-	-
Improved CD	0.910	-	0.830	0.880	-	-	-	-	-	-	-	-	-	-
DoS	0.955	0.995	0.571	-	0.962	1.00	0.965	-	0.949	<u>0.997</u>	0.956	-	0.928	-
WAIC ¹	0.143	0.928	0.532	-	0.802	0.991	0.831	-	0.507	0.139	0.535	-	0.601	-
TT ¹	0.870	0.848	0.548	-	0.970	1.00	0.965	-	0.634	0.982	0.671	-	0.832	-
LR ¹	0.064	0.914	0.520	-	0.819	0.912	0.779	-	0.323	0.028	0.357	-	0.524	-
<i>Diffusion-based</i>														
NLL	0.091	0.574	0.521	0.609	0.990	<u>0.999</u>	0.992	0.983	0.814	0.105	0.786	0.809	0.689	1000
IC	0.921	0.516	0.519	0.553	0.080	0.028	0.100	0.174	0.485	0.972	0.510	0.559	0.451	1000
MSMA	0.957	0.675	0.615	0.967	0.976	0.995	<u>0.980</u>	0.996	0.871	<u>0.997</u>	0.886	0.967	0.907	10
DDPM-OD	0.390	0.659	0.536	0.598	0.951	0.986	0.945	0.910	0.795	0.636	0.778	0.773	0.746	350
LMD	0.992	0.557	0.604	0.667	0.919	0.890	0.881	0.914	0.989	1.00	0.979	<u>0.972</u>	0.865	10 ⁴
<i>Ours</i>														
DiffPath-1D	0.965	<u>0.998</u>	0.551	0.966	0.971	1.00	0.972	0.992	<u>0.998</u>	1.00	0.994	0.827	0.936	<u>50</u>
DiffPath-1D	<u>0.966</u>	0.999	0.552	0.975	0.971	1.00	0.973	0.988	0.999	1.00	0.998	0.851	0.939	100
DiffPath-6D	0.936	0.997	0.596	<u>0.997</u>	0.921	<u>0.999</u>	0.932	<u>0.999</u>	0.997	1.00	<u>0.995</u>	0.935	<u>0.942</u>	<u>50</u>
DiffPath-6D	0.920	0.999	0.593	0.999	0.924	<u>0.999</u>	0.936	1.00	0.999	1.00	0.998	0.946	0.943	100

score function over discrete noise levels for OOD detection. One can view MSMA as a specific case of DiffPath, where the former only utilizes the first-order statistic, while we generalize to higher-order terms. MSMA proposes to measure the score at various noise levels, while our method sums over the entire diffusion path. It is worth emphasizing that MSMA requires different models for different ID tasks, unlike our single model setup.

Reconstruction-based approaches evaluate how well a generative model, trained on ID data, can reconstruct a test sample. Earlier works utilize autoencoders [30] and GANs [31] for reconstruction. Recent works have adapted unconditional DMs to this approach due to its impressive sample quality. A test sample is first artificially corrupted before being reconstructed using the DM’s sampling process. DDPM-OD [7] noises a sample using the forward process and evaluates the perceptual quality [32] of the reconstructed sample. Projection Regret [9] adopts a similar approach, but uses a Consistency Model [33] and introduces an additional projection regret score. LMD [8] corrupts the image by masking and reconstructs the sample via inpainting. Evidently, DiffPath differs from these diffusion approaches as we do not utilize reconstructions. We also stress again that these baselines require different models for different ID tasks.

5 Experiments

Datasets. We evaluate pairwise OOD detection using CIFAR10 (C10), SVHN, and CelebA as ID datasets, and CIFAR100 (C100) and Textures as additional OOD datasets. We employ an unconditional diffusion model trained on ImageNet at 64×64 resolution, using the Improved DDPM’s [34] open-source checkpoint². All datasets are resized to 64×64 when evaluating with DiffPath (see Sec. 5.2 for ablations on resizing techniques).

Methodology and Baselines. Our methodology features two variants of our model, DiffPath-1D using KDE and DiffPath-6D using a Gaussian Mixture Model for OOD scoring, as outlined in Sec. 3.

¹Results obtained from Morningstar et al. [6].

²<https://github.com/openai/improved-diffusion>

Table 4: Ablation results when we vary $p_0(\mathbf{x})$, the distribution the single DM is trained on. We use DiffPath-1D with 50 NFEs. **Bold** and underline denotes the best and second best result.

$p_0(\mathbf{x})$	C10 vs				SVHN vs				CelebA vs				Average
	SVHN	CelebA	C100	Textures	C10	CelebA	C100	Textures	C10	SVHN	C100	Textures	
C10	0.862	0.359	<u>0.538</u>	<u>0.724</u>	0.788	0.807	0.803	0.862	0.658	0.927	0.704	<u>0.839</u>	0.739
SVHN	0.975	0.394	0.512	0.698	0.985	<u>0.997</u>	0.984	<u>0.960</u>	0.625	<u>0.996</u>	0.621	0.779	<u>0.794</u>
CelebA	0.915	<u>0.55</u>	0.519	0.693	0.881	0.779	0.872	0.840	<u>0.772</u>	0.902	<u>0.789</u>	0.850	0.780
ImageNet	<u>0.965</u>	0.998	0.551	0.966	<u>0.971</u>	1.00	<u>0.972</u>	0.992	0.998	1.00	0.994	0.827	0.936

We compare against a variety of generative baselines, including Energy-based Model (EBM) such as IGEBM [28], VAEBM [35] and Improved CD [36], as well as Input Complexity (IC) [16], Density of States (DOS) [6], Watanabe-Akaike Information Criterion (WAIC) [5], Typicality Test (TT) [27] and Likelihood Ratio (LR) [4] applied to the Glow [37] model. Additionally, we compare against diffusion baselines such as vanilla NLL and IC based on the DM’s likelihoods and re-implementations of DDPM-OOD [7], LMD [8], and MSMA [29] based on open-source code for full comparisons.

5.1 Main Results

Table 3 summarizes our main results. Both variants of DiffPath, with 50 and 100 NFEs, obtain the top four best average results across all 12 tasks, with DiffPath-6D at 100 NFEs performing the best. Interestingly, dropping to 50 NFEs only reduces performance marginally while improving inference speed by $2\times$. Specifically, DiffPath-6D at 100 NFEs achieves the best result in six out of twelve tasks, and second best result on one of them, while at 50 NFEs achieves second best result in four out of twelve tasks. Despite using only a scalar statistic for OOD detection, DiffPath-1D at 100 NFEs still obtains the best result in five out of twelve tasks. Thus, our results validate the efficiency and versatility of DiffPath on diverse OOD tasks.

All variants of DiffPath struggle with the C10 vs C100 task due to similarities between these datasets, scoring below 0.7 AUROC. However, this task is also challenging for all baselines, with only Improved CD and IC achieving AUROC scores above 0.7. Interestingly, DiffPath’s performance is strongest when either ID or OOD dataset is CelebA. For instance, we achieve perfect score when distinguishing against SVHN across both variants, and near perfect score (greater than 0.99) against C10/C100. This corroborates the result in Fig. 2, which shows that the histogram of CelebA is well separated from the other datasets.

Interestingly, DiffPath maintains consistent performance when swapping ID and OOD datasets. As a single model is used, the statistics extracted for a dataset is identical (up to differences between train test split) regardless of whether it is ID or OOD. Other methods do not exhibit such behavior as they require different generative models for different tasks. For example, in the C10 vs CelebA/CelebA vs C10 tasks, DiffPath-1D achieves identical scores of 0.999/0.999, while MSMA and LMD achieves scores of 0.675/0.871 and 0.557/0.989 respectively. We believe this symmetry is desirable as it is similar to binary classification, where performance is unchanged when labels are swapped.

DiffPath requires fewer NFEs per sample than most diffusion models, making it faster during inference. Only MSMA uses fewer NFEs, but it performs worse and needs different models for each ID task. Reconstruction-based methods like DDPM-OOD and LMD require many reconstructions per sample, leading to high NFE requirements. In particular, LMD requires a hefty 10^4 NFEs as the original implementation requires 10 reconstructions per sample, with each utilizing 1000 NFEs. As for NLL and IC, both underperform our method despite our experiments showing that roughly 1000 NFEs are required to obtain an accurate estimate of the likelihood.

5.2 Ablations

Choice of Diffusion Training Set. Here we quantitatively justify our claim in Sec. 3.2 that the data distribution used to train the DM, $p_0(\mathbf{x})$, has to be large and diverse for OOD detection. We report ablation results in Table. 4 using DMs trained on CIFAR10, SVHN, CelebA and ImageNet. The results show that the DM trained on ImageNet significantly outperforms the rest, achieving the best

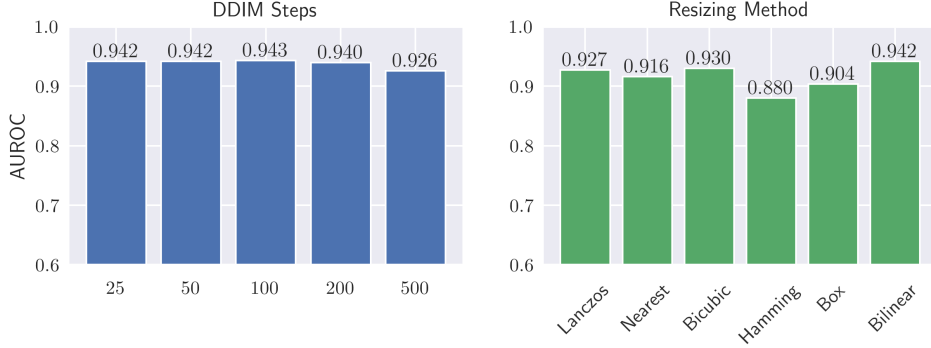


Figure 4: Plots of AUROC performance for various ablation experiments. Average performance over all tasks when the number of DDIM steps is varied (*left*) and when the image resizing technique is varied (*right*). We use DiffPath-6D with 50 NFEs for both. Full results in Sec. B.1 of the appendix.

result across 8 out of 12 tasks, second best on 3 tasks and the best average result by a large margin. This is despite the other variants being trained on samples seen in the experiments, while ImageNet was not. This suggests that it is unnecessary for generative models to be trained on in-distribution data for OOD detection; rather, the model should be trained to learn diverse and general representations.

Number of DDIM Steps. We investigate how the performance of our method varies with the number of DDIM steps used in Fig. 4. Interestingly, the best results are obtained at 25, 50 and 100 DDIM steps, with near identical performance. As the experiments with 50 and 100 steps are more consistent throughout tasks (see Sec. B.1 in appendix for full ablation results), we report results for 50 and 100 NFEs in our main experiments in Table. 3. We hypothesize that the slight decrease in performance at larger DDIM steps is due to the use of the finite difference in Eq. 10, where the difference in consecutive predictions $\epsilon(\cdot, t + \Delta t) - \epsilon(\cdot, t)$ shrinks rapidly. We leave the investigation of this phenomena in greater detail to future work.

Image Resizing Technique. Since we utilize a single DM trained on ImageNet at 64×64 resolution, samples from image distributions of different resolutions have to be resized appropriately. As such, we ablate for resizing techniques that are implemented in the PyTorch library. The results in Fig. 4 show that DiffPath is relatively robust, with average AUROC approximately 0.9 or higher across all resizing techniques considered. However, bicubic and bilinear interpolation outperform the rest, with the latter obtaining the best performance. Thus, we use bilinear interpolation for the experiments described in this work.

6 Conclusion

In this work, we proposed Diffusion Paths (DiffPath), a method of OOD detection using a single diffusion model by characterizing properties of the forward diffusion path. In light of the growing popularity of foundational generative models, our work demonstrates that a generalist model—one that has learnt diverse representations from data—can also be applied to out-of-distribution detection. There are several interesting future directions that arise from our work; for instance, applying DiffPath to other modalities, given that diffusion modelling has been extended to domains such as video, audio, language and time series, as well as investigating if higher-order terms in the Taylor expansion, or leveraging different instantiations of the PF ODE might lead to better performance. We hope that our work sparks greater interest among practitioners in utilizing other foundational generative models beyond DMs for OOD detection, such as large language models.

Limitations and Future Work. We only calculate the simple time derivative and found that it works well experimentally, although one might compute the full derivative to quantify the curvature completely. We leave this for future work. Also, we consider a DM trained on ImageNet, which may not be general enough for specialized applications such as medical images. For such purposes, one could consider including domain-specific data when training the DM, or utilize larger DMs such as Stable Diffusion.

7 Acknowledgements

We would like to thank Pranav Goyal for help with the experiments. This research is supported by the National Research Foundation Singapore and DSO National Laboratories under the AI Singapore Programme (AISG Award No: AISG2-RP-2020-017).

References

- [1] Anh Nguyen, Jason Yosinski, and Jeff Clune. Deep neural networks are easily fooled: High confidence predictions for unrecognizable images. In *Proceedings of the IEEE conference on computer vision and pattern recognition*, pages 427–436, 2015.
- [2] Eric Nalisnick, Akihiro Matsukawa, Yee Whye Teh, Dilan Gorur, and Balaji Lakshminarayanan. Do deep generative models know what they don’t know? In *International Conference on Learning Representations*, 2018.
- [3] Jingkan Yang, Kaiyang Zhou, Yixuan Li, and Ziwei Liu. Generalized out-of-distribution detection: A survey. *arXiv preprint arXiv:2110.11334*, 2021.
- [4] Jie Ren, Peter J Liu, Emily Fertig, Jasper Snoek, Ryan Poplin, Mark Depristo, Joshua Dillon, and Balaji Lakshminarayanan. Likelihood ratios for out-of-distribution detection. *Advances in neural information processing systems*, 32, 2019.
- [5] Hyunsun Choi, Eric Jang, and Alexander A Alemi. Waic, but why? generative ensembles for robust anomaly detection. *arXiv preprint arXiv:1810.01392*, 2018.
- [6] Warren Morningstar, Cusuh Ham, Andrew Gallagher, Balaji Lakshminarayanan, Alex Alemi, and Joshua Dillon. Density of states estimation for out of distribution detection. In *International Conference on Artificial Intelligence and Statistics*, pages 3232–3240. PMLR, 2021.
- [7] Mark S Graham, Walter HL Pinaya, Petru-Daniel Tudosiu, Parashkev Nachev, Sebastien Ourselin, and Jorge Cardoso. Denoising diffusion models for out-of-distribution detection. In *Proceedings of the IEEE/CVF Conference on Computer Vision and Pattern Recognition*, pages 2947–2956, 2023.
- [8] Zhenzhen Liu, Jin Peng Zhou, Yufan Wang, and Kilian Q Weinberger. Unsupervised out-of-distribution detection with diffusion inpainting. In *International Conference on Machine Learning*, pages 22528–22538. PMLR, 2023.
- [9] Sungik Choi, Hankook Lee, Honglak Lee, and Moontae Lee. Projection regret: Reducing background bias for novelty detection via diffusion models. *Advances in Neural Information Processing Systems*, 36, 2024.
- [10] Zhisheng Xiao, Qing Yan, and Yali Amit. Do we really need to learn representations from in-domain data for outlier detection? *arXiv preprint arXiv:2105.09270*, 2021.
- [11] Tom Brown, Benjamin Mann, Nick Ryder, Melanie Subbiah, Jared D Kaplan, Prafulla Dhariwal, Arvind Neelakantan, Pranav Shyam, Girish Sastry, Amanda Askell, et al. Language models are few-shot learners. *Advances in neural information processing systems*, 33:1877–1901, 2020.
- [12] Rishi Bommasani, Drew A Hudson, Ehsan Adeli, Russ Altman, Simran Arora, Sydney von Arx, Michael S Bernstein, Jeannette Bohg, Antoine Bosselut, Emma Brunskill, et al. On the opportunities and risks of foundation models. *arXiv preprint arXiv:2108.07258*, 2021.
- [13] Yang Song, Jascha Sohl-Dickstein, Diederik P Kingma, Abhishek Kumar, Stefano Ermon, and Ben Poole. Score-based generative modeling through stochastic differential equations. In *International Conference on Learning Representations*, 2020.
- [14] Yang Song and Stefano Ermon. Generative modeling by estimating gradients of the data distribution. *Advances in neural information processing systems*, 32, 2019.
- [15] Jonathan Ho, Ajay Jain, and Pieter Abbeel. Denoising diffusion probabilistic models. *Advances in neural information processing systems*, 33:6840–6851, 2020.
- [16] Joan Serrà, David Álvarez, Vicenç Gómez, Olga Slizovskaia, José F Núñez, and Jordi Luque. Input complexity and out-of-distribution detection with likelihood-based generative models. In *International Conference on Learning Representations*, 2019.
- [17] Aapo Hyvärinen and Peter Dayan. Estimation of non-normalized statistical models by score matching. *Journal of Machine Learning Research*, 6(4), 2005.

- [18] Tim Dockhorn, Arash Vahdat, and Karsten Kreis. Genie: Higher-order denoising diffusion solvers. *Advances in Neural Information Processing Systems*, 35:30150–30166, 2022.
- [19] Jiaming Song, Chenlin Meng, and Stefano Ermon. Denoising diffusion implicit models. In *International Conference on Learning Representations*, 2020.
- [20] Peter E. Kloeden and Eckhard Platen. *Numerical Solution of Stochastic Differential Equations*. Springer, Berlin, 1992.
- [21] Valentin Khrulkov, Gleb Ryzhakov, Andrei Chertkov, and Ivan Oseledets. Understanding ddpm latent codes through optimal transport. In *The Eleventh International Conference on Learning Representations*, 2022.
- [22] Xuan Su, Jiaming Song, Chenlin Meng, and Stefano Ermon. Dual diffusion implicit bridges for image-to-image translation. In *The Eleventh International Conference on Learning Representations*, 2022.
- [23] Simo Särkkä and Arno Solin. *Applied stochastic differential equations*, volume 10. Cambridge University Press, 2019.
- [24] Taylor Denouden, Rick Salay, Krzysztof Czarnecki, Vahdat Abdelzad, Buu Phan, and Sachin Vernekar. Improving reconstruction autoencoder out-of-distribution detection with mahalanobis distance. *arXiv preprint arXiv:1812.02765*, 2018.
- [25] Jihoon Tack, Sangwoo Mo, Jongheon Jeong, and Jinwoo Shin. Csi: Novelty detection via contrastive learning on distributionally shifted instances. *Advances in neural information processing systems*, 33: 11839–11852, 2020.
- [26] Vikash Sehwal, Mung Chiang, and Prateek Mittal. Ssd: A unified framework for self-supervised outlier detection. *arXiv preprint arXiv:2103.12051*, 2021.
- [27] Eric Nalisnick, Akihiro Matsukawa, Yee Whye Teh, and Balaji Lakshminarayanan. Detecting out-of-distribution inputs to deep generative models using typicality. *arXiv preprint arXiv:1906.02994*, 2019.
- [28] Yilun Du and Igor Mordatch. Implicit generation and modeling with energy based models. *Advances in Neural Information Processing Systems*, 32, 2019.
- [29] Ahsan Mahmood, Junier Oliva, and Martin Andreas Styner. Multiscale score matching for out-of-distribution detection. In *International Conference on Learning Representations*, 2020.
- [30] Chong Zhou and Randy C Paffenroth. Anomaly detection with robust deep autoencoders. In *Proceedings of the 23rd ACM SIGKDD international conference on knowledge discovery and data mining*, pages 665–674, 2017.
- [31] Thomas Schlegl, Philipp Seeböck, Sebastian M Waldstein, Ursula Schmidt-Erfurth, and Georg Langs. Unsupervised anomaly detection with generative adversarial networks to guide marker discovery. In *International conference on information processing in medical imaging*, pages 146–157. Springer, 2017.
- [32] Richard Zhang, Phillip Isola, Alexei A Efros, Eli Shechtman, and Oliver Wang. The unreasonable effectiveness of deep features as a perceptual metric. In *Proceedings of the IEEE conference on computer vision and pattern recognition*, pages 586–595, 2018.
- [33] Yang Song, Prafulla Dhariwal, Mark Chen, and Ilya Sutskever. Consistency models. In *International Conference on Machine Learning*, pages 32211–32252. PMLR, 2023.
- [34] Alexander Quinn Nichol and Prafulla Dhariwal. Improved denoising diffusion probabilistic models. In *International conference on machine learning*, pages 8162–8171. PMLR, 2021.
- [35] Zhisheng Xiao, Karsten Kreis, Jan Kautz, and Arash Vahdat. Vaeblm: A symbiosis between variational autoencoders and energy-based models. In *International Conference on Learning Representations*, 2020.
- [36] Yilun Du, Shuang Li, Joshua Tenenbaum, and Igor Mordatch. Improved contrastive divergence training of energy-based models. In *International Conference on Machine Learning*, pages 2837–2848. PMLR, 2021.
- [37] Durk P Kingma and Prafulla Dhariwal. Glow: Generative flow with invertible 1x1 convolutions. *Advances in neural information processing systems*, 31, 2018.
- [38] Yang Song, Conor Durkan, Iain Murray, and Stefano Ermon. Maximum likelihood training of score-based diffusion models. *Advances in neural information processing systems*, 34:1415–1428, 2021.
- [39] Gabriel Peyré and Marco Cuturi. Computational optimal transport. *Foundations and Trends in Machine Learning*, 11(5-6):355–607, 2019.

Supplementary Material for “Out-of-Distribution Detection with a Single Unconditional Diffusion Model”

A Proofs

A.1 Theorem 1

Theorem 1. Denote ϕ_t and ψ_t as the marginals from evolving two distinct distributions ϕ_0 and ψ_0 via their respective probability flow ODEs (Eq. 6) forward in time. We consider the case with the same forward process, i.e., the two PF ODEs have the same $\mathbf{f}(\mathbf{x}_t, t)$, $g(t)$ and σ_t . Under some regularity conditions stated in Appendix A.1,

$$D_{\text{KL}}(\phi_0 \parallel \psi_0) = \frac{1}{2} \int_0^T \mathbb{E}_{\mathbf{x} \sim \phi_t} \frac{g(t)^2}{\sigma_t} \|\epsilon_\phi(\mathbf{x}_t, t) - \epsilon_\psi(\mathbf{x}_t, t)\|_2^2 dt + D_{\text{KL}}(\phi_T \parallel \psi_T).$$

Proof. The proof is a modification from Song et al. [38]. Let us first state the PF ODEs of the two distributions explicitly:

$$\frac{d\mathbf{x}_t}{dt} = \mathbf{f}(\mathbf{x}_t, t) + \frac{g(t)^2}{2\sigma_t} \epsilon_\phi(\mathbf{x}_t, t), \quad \epsilon_\phi(\mathbf{x}_t, t) = -\sigma_t \nabla_{\mathbf{x}} \log \phi_t(\mathbf{x}) \quad (11)$$

$$\frac{d\mathbf{x}_t}{dt} = \mathbf{f}(\mathbf{x}_t, t) + \frac{g(t)^2}{2\sigma_t} \epsilon_\psi(\mathbf{x}_t, t), \quad \epsilon_\psi(\mathbf{x}_t, t) = -\sigma_t \nabla_{\mathbf{x}} \log \psi_t(\mathbf{x}). \quad (12)$$

We make the following assumption about ϕ_t and ψ_t :

$$\forall t \in [0, T] \exists k > 0 \text{ s.t. } \phi_t(\mathbf{x}) = O(e^{-\|\mathbf{x}\|_2^k}), \quad \psi_t(\mathbf{x}) = O(e^{-\|\mathbf{x}\|_2^k}) \text{ as } \|\mathbf{x}\|_2 \rightarrow \infty. \quad (13)$$

This assumption essentially states that both marginals have at most polynomial growth at infinity and thus can be normalized.

We start by rewriting the KL divergence between ϕ_0 and ψ_0 in integral form:

$$\begin{aligned} D_{\text{KL}}(\phi_0 \parallel \psi_0) &= D_{\text{KL}}(\phi_0 \parallel \psi_0) - D_{\text{KL}}(\phi_T \parallel \psi_T) + D_{\text{KL}}(\phi_T \parallel \psi_T) \\ &= - \int_0^T \frac{\partial D_{\text{KL}}(\phi_t \parallel \psi_t)}{\partial t} dt + D_{\text{KL}}(\phi_T \parallel \psi_T). \end{aligned} \quad (14)$$

As we can treat the PF ODE as a special case of an SDE with zero diffusion term, we can obtain the Fokker-Planck of the marginal density of the PF ODEs, also known as the continuity equation, as follows:

$$\frac{\partial \phi_t}{\partial t} = \nabla_{\mathbf{x}} \cdot \left(-\mathbf{f}(\mathbf{x}_t, t) \phi_t(\mathbf{x}) - \frac{g(t)^2}{2\sigma_t} \epsilon_\phi(\mathbf{x}_t, t) \phi_t(\mathbf{x}) \right) = \nabla_{\mathbf{x}} \cdot (\mathbf{h}_\phi \phi_t(\mathbf{x})) \quad (15)$$

where we define $\mathbf{h}_\phi := -\mathbf{f}(\mathbf{x}_t, t) - \frac{g(t)^2}{2\sigma_t} \epsilon_\phi(\mathbf{x}_t, t)$ for simplicity. Similarly, $\frac{\partial \psi_t}{\partial t} = \nabla_{\mathbf{x}} \cdot (\mathbf{h}_\psi \psi_t(\mathbf{x}))$.

Let us now rewrite the time-derivative $\frac{\partial D_{\text{KL}}(\phi_t \parallel \psi_t)}{\partial t}$ in Eq. 14 as follows:

$$\begin{aligned} \frac{\partial D_{\text{KL}}(\phi_t \parallel \psi_t)}{\partial t} &= \frac{\partial}{\partial t} \int \phi_t(\mathbf{x}) \log \frac{\phi_t(\mathbf{x})}{\psi_t(\mathbf{x})} d\mathbf{x} \\ &= \int \frac{\partial \phi_t}{\partial t} \log \frac{\phi_t(\mathbf{x})}{\psi_t(\mathbf{x})} d\mathbf{x} + \underbrace{\int \frac{\partial \phi_t(\mathbf{x})}{\partial t} d\mathbf{x}}_{=0} - \int \frac{\phi_t(\mathbf{x})}{\psi_t(\mathbf{x})} \frac{\partial \psi_t(\mathbf{x})}{\partial t} d\mathbf{x} \\ &= \int \nabla_{\mathbf{x}} \cdot (\mathbf{h}_\phi(\mathbf{x}, t) \phi_t(\mathbf{x})) \log \frac{\phi_t(\mathbf{x})}{\psi_t(\mathbf{x})} d\mathbf{x} - \int \frac{\phi_t(\mathbf{x})}{\psi_t(\mathbf{x})} \nabla_{\mathbf{x}} \cdot (\mathbf{h}_\psi(\mathbf{x}, t) \psi_t(\mathbf{x})) d\mathbf{x} \\ &\stackrel{(i)}{=} \int \phi_t(\mathbf{x}) [\mathbf{h}_\phi^\top(\mathbf{x}, t) - \mathbf{h}_\psi^\top(\mathbf{x}, t)] [\nabla_{\mathbf{x}} \log \phi_t(\mathbf{x}) - \nabla_{\mathbf{x}} \log \psi_t(\mathbf{x})] d\mathbf{x} \\ &= -\frac{1}{2} \int \phi_t(\mathbf{x}) \frac{g(t)^2}{\sigma_t} \|\epsilon_\phi(\mathbf{x}, t) - \epsilon_\psi(\mathbf{x}, t)\|_2^2 d\mathbf{x}, \end{aligned}$$

where (i) is due to integration by parts and the fact that $\lim_{\mathbf{x} \rightarrow \infty} \mathbf{h}_\phi(\mathbf{x}, t) \phi_t(\mathbf{x}) = 0$ and $\lim_{\mathbf{x} \rightarrow \infty} \mathbf{h}_\psi(\mathbf{x}, t) \psi_t(\mathbf{x}) = 0$ due to assumption 13. Combining with Eq. 14 gives us the desired result:

$$D_{\text{KL}}(\phi_0 \parallel \psi_0) = \frac{1}{2} \int_0^T \mathbb{E}_{x \sim \phi_t} \frac{g(t)^2}{\sigma_t} \|\epsilon_\phi(\mathbf{x}_t, t) - \epsilon_\psi(\mathbf{x}_t, t)\|_2^2 dt + D_{\text{KL}}(\phi_T \parallel \psi_T). \quad (16)$$

□

A.2 OT Toy Example

We derive here in detail the toy example discussed in Sec. 3.4, where we will prove the optimal transport map between a multivariate Gaussian and standard normal is identical to the diffusion PF ODE path. We consider our source distribution as $p_0(\mathbf{x}) \sim \mathcal{N}(\mathbf{a}, \mathbf{I})$, $\mathbf{a} \in \mathbb{R}^d$ and $\mathbf{I} \in \mathbb{R}^{d \times d}$. We choose our forward SDE to be parameterized as:

$$d\mathbf{x}_t = -\mathbf{x}_t dt + \sqrt{2} d\mathbf{w}_t, \quad (17)$$

which is the same Ornstein–Uhlenbeck process as the DDPM forward SDE Eq. 4 with a constant noise schedule $\beta(t) = 2$. This is also commonly referred to as the Langevin equation.

As Eq. 17 has affine drift coefficients and a starting distribution which is normal, we know that the marginal distributions at intermediate times are also normal, $p_t(\mathbf{x}) \sim \mathcal{N}(\boldsymbol{\mu}(t), \boldsymbol{\Sigma}(t))$. Furthermore, we can calculate the means and variances analytically using Eq. 5.50 and Eq. 5.51 of Särkkä and Solin [23]:

$$\frac{d\boldsymbol{\mu}(t)}{dt} = -\boldsymbol{\mu}(t), \quad \frac{d\boldsymbol{\Sigma}(t)}{dt} = -2\boldsymbol{\Sigma}(t) + 2 \quad (18)$$

with solutions

$$\boldsymbol{\mu}(t) = \boldsymbol{\mu}(0)e^{-t} = \mathbf{a}e^{-t}, \quad \boldsymbol{\Sigma}(t) = \mathbf{I} + e^{-2t}(\boldsymbol{\Sigma}(0) - \mathbf{I}) = \mathbf{I}. \quad (19)$$

Thus, the marginal density has the form $p_t(\mathbf{x}) = \mathcal{N}(\mathbf{a}e^{-t}, \mathbf{I})$, from which we compute the score as $\nabla_{\mathbf{x}} \log p_t(\mathbf{x}) = -\mathbf{x} + \mathbf{a}e^{-t}$. We can substitute this into the corresponding PF ODE to obtain:

$$\begin{aligned} \frac{d\mathbf{x}_t}{dt} &= -\mathbf{x} - \nabla_{\mathbf{x}} \log p_t(\mathbf{x}) \\ &= -\mathbf{a}e^{-t}. \end{aligned} \quad (20)$$

The optimal transport map denoted $E_{p_0}(\mathbf{x})$ is obtained by solving Eq. 20 to get $\mathbf{x}_t = \mathbf{x}_0 + \mathbf{a}(e^{-t} - \mathbf{I})$ and taking the limit $t \rightarrow \infty$. This gives us $E_{p_0}(\mathbf{x}) = \mathbf{x} - \mathbf{a}$, which is precisely the OT map between $p_0(\mathbf{x}) \sim \mathcal{N}(\mathbf{a}, \mathbf{I})$ and $\mathcal{N}(\mathbf{0}, \mathbf{I})$ (cf. Eq. 2.40 in Peyré and Cuturi [39]).

B Experimental Details

DiffPath As mentioned in Sec. 5, we utilize a single unconditional diffusion model trained on ImageNet at 64×64 resolution. The checkpoint that we use is trained using Improved DDPM’s L_{hybrid} objective (Eq. 16 of Nichol and Dhariwal [34]). The model uses a cosine noise schedule with a total of 4000 diffusion steps. The checkpoint is publicly available on the official GitHub repository³. For DiffPath-1D, we fit a KDE using a Gaussian kernel with a bandwidth of 5. For DiffPath-6D, we fit a GMM using 50 mixture components, each with diagonal covariance. Both are implemented using the `sklearn` library. We calculate the diffusion statistics using a single A5000 GPU.

Diffusion Baselines For all diffusion baselines, we rely on the official GitHub repositories and open-source checkpoints where possible. The repositories are listed as follows: MSMA⁴, DDPM-OOD⁵, LMD⁶. For NLL and IC, we either use the pre-trained CIFAR10 checkpoint from Improved DDPM or train separate models for SVHN and CelebA using the same hyperparameters at 32×32 resolution. We calculate the NLL using the default implementation in Improved DDPM, while we compute IC using code from the LR repository⁷ due to lack of official code from the IC authors. We train all baselines using 1-3 A5000 GPUs.

³<https://github.com/openai/improved-diffusion>

⁴<https://github.com/ahsanMah/msma>

⁵<https://github.com/marksgraham/ddpm-ood>

⁶https://github.com/zhenzhel/lift_map_detect

⁷<https://github.com/XavierXiao/Likelihood-Regret>

Table 5: Full ablation results when we vary the number of DDIM steps (NFE). We use DiffPath-6D. **Bold** and underline denotes the best and second best result.

NFE	C10 vs				SVHN vs				CelebA vs				Average
	SVHN	CelebA	C100	Textures	C10	CelebA	C100	Textures	C10	SVHN	C100	Textures	
25	0.917	0.996	0.587	0.997	0.919	<u>0.999</u>	0.929	1	0.995	1	0.993	0.970	<u>0.942</u>
50	0.936	0.997	0.596	0.997	<u>0.921</u>	<u>0.999</u>	<u>0.932</u>	<u>0.999</u>	<u>0.997</u>	1	0.995	0.935	<u>0.942</u>
100	<u>0.920</u>	<u>0.999</u>	<u>0.593</u>	0.999	0.924	<u>0.999</u>	0.936	1	0.999	1	<u>0.998</u>	0.946	0.943
200	0.882	1	0.588	0.999	0.912	1	0.926	1	0.999	1	0.999	<u>0.973</u>	0.940
500	0.834	<u>0.999</u>	0.583	0.999	0.850	1	0.870	1	0.999	1	<u>0.998</u>	0.981	0.926

Table 6: Full ablation results when we vary the resizing method of the images. We use DiffPath-6D. **Bold** and underline denotes the best and second best result.

Resizing Method	C10 vs				SVHN vs				CelebA vs				Average
	SVHN	CelebA	C100	Textures	C10	CelebA	C100	Textures	C10	SVHN	C100	Textures	
Lanczos	0.819	0.997	<u>0.593</u>	<u>0.994</u>	0.891	<u>0.996</u>	0.910	<u>0.996</u>	0.997	1	0.996	0.937	0.927
Nearest	0.815	<u>0.995</u>	0.575	0.973	0.836	0.999	0.865	0.993	0.979	<u>0.995</u>	0.983	0.983	0.916
Bicubic	<u>0.900</u>	0.988	0.589	0.987	<u>0.899</u>	0.994	<u>0.916</u>	<u>0.996</u>	<u>0.986</u>	1	0.979	0.930	<u>0.930</u>
Hamming	0.823	0.898	0.575	0.937	0.852	0.990	0.877	0.985	0.835	0.986	0.862	<u>0.938</u>	0.880
Box	0.814	0.974	0.574	0.957	0.835	0.995	0.866	0.991	0.951	0.987	0.962	<u>0.938</u>	0.904
Bilinear	0.936	0.997	0.596	0.997	0.921	0.999	0.932	0.999	0.997	1	<u>0.995</u>	0.935	0.942

B.1 Full Results for Ablations

We provide full results of the ablations presented in Fig. 4 in Table 5 and Table 6. When varying the NFE in Table 5, we observe that certain tasks are more sensitive than others, although the average across all tasks is much more stable. For instance, the worst performance between CIFAR10 vs SVHN has AUROC of 0.834 at 500 steps, while the best performance has AUROC of 0.936 at 50 steps. However, other tasks remain unchanged when NFE is varied, such as SVHN vs Textures or CelebA vs SVHN. We generally find 50 and 100 steps to the sweet spot.

When the resizing method is varied in Table 6, we find bicubic and bilinear interpolation to perform significantly better than the rest, with bilinear achieving the best scores in most tasks. As such, we use bilinear in all other experiments in the main text.